



Nightside Winds at the Lower Clouds of Venus with *Akatsuki*/IR2: Longitudinal, Local Time, and Decadal Variations from Comparison with Previous Measurements

Javier Peralta¹, Keishiro Muto², Ricardo Hueso³, Takeshi Horinouchi⁴, Agustín Sánchez-Lavega³, Shin-ya Murakami¹, Pedro Machado⁵, Eliot F. Young⁶, Yeon Joo Lee², Toru Kouyama⁷, Hideo Sagawa⁸, Kevin McGouldrick⁹, Takehiko Satoh^{1,10}, Takeshi Imamura², Sanjay S. Limaye¹¹, Takao M. Sato^{1,12}, Kazunori Ogohara¹³, Masato Nakamura¹, and David Luz⁵

¹ Institute of Space and Astronautical Science (ISAS), Japan Aerospace Exploration Agency (JAXA) 3-1-1, Yoshinodai, Chuo-ku, Sagami-hara, Kanagawa, 252-5210, Japan; javier.peralta@ac.jaxa.jp

² Graduate School of Frontier Sciences, The University of Tokyo, Japan

³ Escuela de Ingeniería de Bilbao (UPV/EHU), Bilbao, Spain

⁴ Faculty of Environmental Earth Science, Hokkaido University, Sapporo, Japan

⁵ Institute of Astrophysics and Space Sciences, Portugal

⁶ Southwest Research Institute, Boulder, CO 80302, USA

⁷ Artificial Intelligence Research Center, National Institute of Advanced Industrial Science and Technology, Tokyo, Japan

⁸ Faculty of Science, Kyoto Sangyo University, Japan

⁹ Laboratory for Atmospheric and Space Physics, University of Colorado Boulder, Boulder, CO 80303-7814, USA

¹⁰ Department of Space and Astronautical Science, School of Physical Sciences, Soken-dai, Japan

¹¹ Space Science and Engineering Center, University of Wisconsin-Madison, Madison, USA

¹² Space Information Center, Hokkaido Information University, Hokkaido, Japan

¹³ School of Engineering, University of Shiga Prefecture, Shiga, Japan

Received 2018 June 19; revised 2018 October 3; accepted 2018 October 11; published 2018 December 7

Abstract

We present measurements of the wind speeds at the nightside lower clouds of Venus from observations by JAXA's mission *Akatsuki* during 2016, complemented by new wind measurements from ground-based observations acquired with the TNG/Near Infrared Camera Spectrometer (NICS) in 2012 and IRTF/SpeX in 2015 and 2017. The zonal and meridional components of the winds were measured via cloud tracking on a total of 466 *Akatsuki* images of Venus acquired by the camera IR2 using the 2.26 μm filter, with spatial resolutions ranging from 10 to 80 km per pixel and covering 2016 March 22 to October 31. More than 149,000 wind vectors were obtained using an automatic template-matching technique, and 2947 wind vectors were inferred using a manual procedure. The meridional profiles for both components of the winds are found to be consistent with results from the *Venus Express* mission during 2006–2008, although stronger wind variability is found for the zonal component at equatorial latitudes where *Akatsuki* observations have better viewing geometry than *Venus Express*. The zonal winds at low latitudes also suggest a zonal variability that could be associated with solar tides or vertically propagating orographic waves. Finally, the combination of our wind measurements from TNG/NICS, IRTF/SpeX, and *Akatsuki* images with previously published data from 1978 to 2017 suggests variations of up to 30 m s^{-1} in the winds at the nightside lower clouds of Venus.

Key words: planets and satellites: atmospheres – planets and satellites: terrestrial planets

Supporting material: tar.gz file

1. Introduction

The atmospheric circulation of Venus from the surface up to the stratosphere is dominated by retrograde zonal superrotation (hereafter RZS), which, according to both in situ (Counselman et al. 1980) and cloud tracking measurements (Sánchez-Lavega et al. 2008), attains the fastest wind speeds at the top of Venus's cloud layer (Schubert 1983; Gierasch et al. 1997; Sánchez-Lavega et al. 2017). The cloud layer is also where most of the energy from solar radiation is deposited (Lee et al. 2015b), so a detailed characterization of the atmospheric circulation at different levels of the clouds (Sánchez-Lavega et al. 2008; Peralta et al. 2017b) seems essential to properly evaluate the sources and transport of angular momentum in the atmosphere. The wind speeds at the upper clouds of Venus (60–70 km above

the surface) are customarily characterized by cloud tracking on both day- (Rossow et al. 1990; Belton et al. 1991; Limaye 2007; Peralta et al. 2007; Khatuntsev et al. 2013; Kouyama et al. 2013; Hueso et al. 2015; Horinouchi et al. 2018) and nightsides (Peralta et al. 2017a), while the winds at the deeper middle and lower clouds (about 48–60 km) have been evaluated following cloud features visible on the dayside of the planet on the near-infrared-wavelength albedo (Belton et al. 1991; Hueso et al. 2015; Khatuntsev et al. 2017) and in the lower clouds on the nightside (Sánchez-Lavega et al. 2008; Hueso et al. 2012; Horinouchi et al. 2017a), thanks to inhomogeneities in the opacity of the lower clouds, which can be observed at the infrared windows at 1.7 and 2.2–2.3 μm (Peralta et al. 2017c).

After the discovery of these infrared spectral windows by Allen & Crawford (1984) and before the arrival of *Akatsuki* (Nakamura et al. 2016), ESA's *Venus Express* mission (hereafter *VEx*) characterized the RZS at the deeper clouds with unprecedented detail during 2006–2008. However, constraints due to *VEx*'s polar orbit (Titov et al. 2006) and



Original content from this work may be used under the terms of the [Creative Commons Attribution 3.0 licence](https://creativecommons.org/licenses/by/3.0/). Any further distribution of this work must maintain attribution to the author(s) and the title of the work, journal citation and DOI.

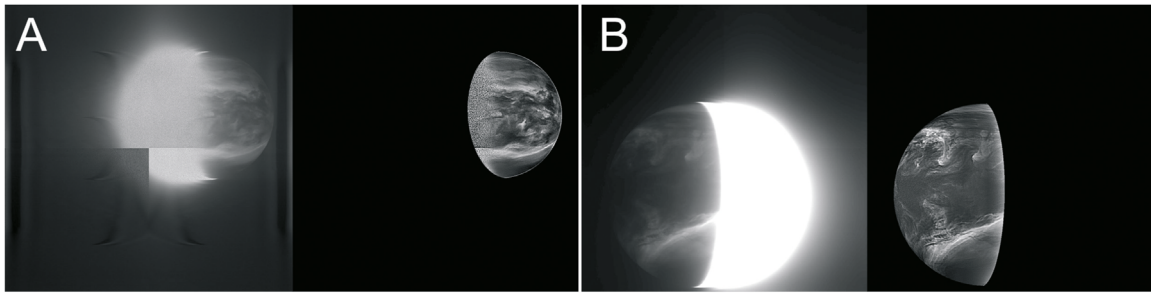


Figure 1. Examples of the IR2/2.26 μm images before and after the processing procedure described in this work. (A) IR2 image acquired on March 25, 11:33 UT, and (B) IR2 image acquired on August 25, 04:03 UT. Both images have been oriented so that the north–south–west–east of Venus appears approximately oriented up–down–left–right in the image.

the long exposure times required by the imaging spectrometer VIRTIS-M (Piccioni et al. 2007) limited observations to the southern hemisphere of Venus with lower quality results at the equatorial and lower latitudes (Sánchez-Lavega et al. 2008; Hueso et al. 2012; McGouldrick et al. 2012; Peralta et al. 2017b). As a result, the circulation at the level of the deeper clouds is poorly characterized in the northern hemisphere where only sparse measurements exist from ground-based observations (Crisp et al. 1989, 1991; Chanover et al. 1998; Limaye et al. 2006) and images from the Near-Infrared Mapping Spectrometer (NIMS) instrument during the flyby of NASA’s *Galileo* in 1990 (Carlson et al. 1991). Since its orbit insertion in 2015 December, JAXA’s *Akatsuki* orbiter has provided an invaluable opportunity to study this deeper atmospheric circulation on both hemispheres thanks to its equatorial orbit (Nakamura et al. 2016) and the images provided by the 2 μm camera IR2 (Satoh et al. 2016).

In this work, we present the first global measurements of the wind speeds at the nightside lower clouds of Venus during the first year of *Akatsuki* observations. A description of the observations performed by the IR2 camera, the processing of the images, navigation corrections, and methods of cloud tracking are introduced in Section 2. The lower clouds’ morphologies, the meridional profiles of the wind speeds, and the possible relation between morphologies and speeds are presented in Section 3. The wind speeds’ dependence on the size and opacity of the clouds and on the local time, and possible relations with the surface topography are studied in Section 4, while the temporal variation of the winds of the lower clouds is presented in Section 5. Finally, the main conclusions of this work are presented in Section 6.

2. Methods

After failing its originally planned orbit insertion in 2010 December 7, *Akatsuki* orbited the Sun for five years and was successfully inserted into the orbit of Venus in 2015 December (Nakamura et al. 2016). At present, the orbiter follows a westward equatorial orbit with an apoapsis of $\sim 360,000$ km, periapsis ranging from 1000 to 8000 km, and a rotation period of about 10 days. Among its payload, the camera IR2 was designed to sense the deep clouds of Venus and infer information about the atmospheric compounds below the cloud layer, thanks to its narrowband filters centered at 1.74, 2.26, and 2.32 μm (Satoh et al. 2016). The scientific objectives of these filters include the study of the morphology of the clouds and their motions, the aerosols’ properties, or the abundance of the CO below the clouds (Satoh et al. 2017). Because of the highly eccentric orbit of *Akatsuki*, the spatial resolution of

Venus in the IR2 images varies from 74 to 12 km per pixel for off-pericenter observations, to 1.6–0.2 km during pericentric ones (Nakamura et al. 2016). Unfortunately, the acquisition of IR2 images was indefinitely interrupted in 2016 December 9 when the electronic device controlling the IR1 and IR2 cameras started to experience an unstable power consumption that has persisted through the present time (Iwagami et al. 2018).

In addition to the IR2 images, new wind measurements have been obtained in this work with ground-based images of Venus acquired after the failure of the infrared channel of the VIRTIS-M (Hueso et al. 2012) instrument on *VEx* and before and after the time period covered by the *Akatsuki* IR2 observations. The Near Infrared Camera Spectrometer (NICS; Baffa et al. 2001) at the Italian National Telescope Galileo (TNG) at La Palma (Canary Islands, Spain) was used to acquire images of the nightside of Venus during 2012 July 11–13 (Mota Machado et al. 2016), while the Medium-Resolution 0.8–5.5 Micron Spectrograph and Imager (SpeX; Rayner et al. 2003) at the 3 m National Aeronautics and Space Administration Infrared Telescope Facility (IRTF) was used to provide images of Venus with the *K*-continuum filter in 2015 September and 2017 January–February (Lee et al. 2017a). The wind measurements from these ground-based images will be presented in Section 5.

2.1. Image Processing

IR2 acquired a total of 1671 images¹⁴ of the nightside of Venus with the filters 1.74, 2.26, and 2.32 μm (Satoh et al. 2017), among which ~ 1370 were regarded as suitable for cloud tracking. Satoh et al. (2017, Figure 8(a) therein) reported a problem of light contamination in the IR2 images, consisting of the presence of halation rings and a cross pattern extending both horizontally and vertically around the saturated dayside of Venus and spreading with multiple reflections along the PtSi detector. Since this contamination is more reduced in the images taken with the 2.26 μm filter, we restricted our cloud tracking study to this data set composed of 466 images (although additional sets with 1.74 μm images were used in the case of automated cloud tracking). The calibration version of the IR2 images used in this work (“v20170601”) does not include any of the corrections for the light contamination proposed by Satoh et al. (2017), and an alternative image processing technique was applied. This consisted of an adjustment of the brightness/contrast, followed by a sharpening of the images with an unsharp-mask technique, and

¹⁴ Available at <http://darts.isas.jaxa.jp/planet/project/akatsuki/>.

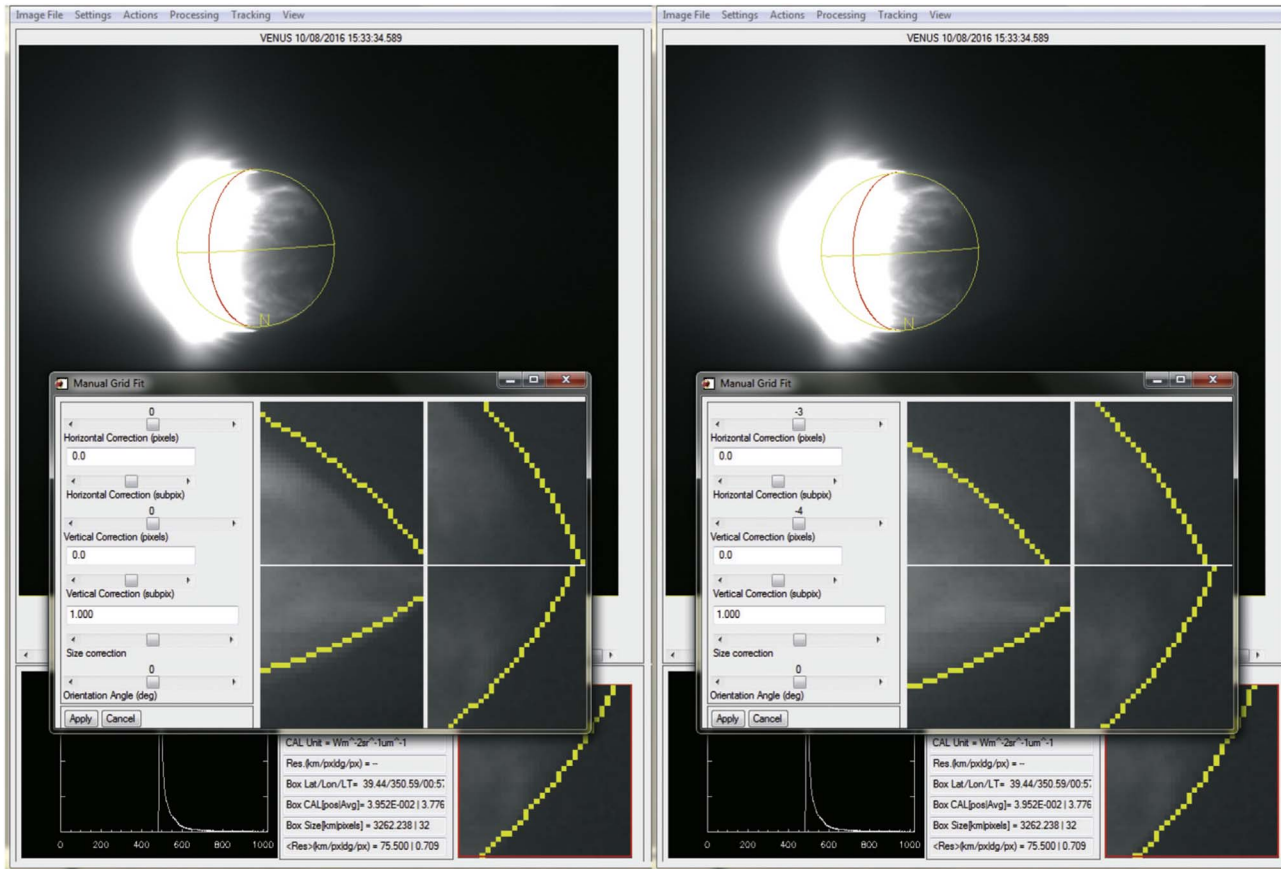


Figure 2. Example of the correction of the navigation of *Akatsuki* images using as reference a set of locations on the planetary limb selected by the user. The original navigation grid and the corrected one are displayed on the left and right sides, respectively.

finishing with the application of adaptive histogram equalization (see examples in Figure 1). Images acquired with ground-based instruments at TNG and IRTF also suffered from contamination from the illuminated side of the planet and were processed similarly. Some examples of these images are shown in Section 5.

2.2. Navigation of IR2 and Ground-based Images

Uncertainties such as the thermal distortion affecting the *Akatsuki* spacecraft and the onboard cameras prevent high accuracy in the navigation of the Venus images at present, so additional corrections in the navigation are still required (Ogohara et al. 2017; Satoh et al. 2017). In recently published studies with *Akatsuki* (Fukuhara et al. 2017; Horinouchi et al. 2017a, 2018; Lee et al. 2017b), the navigation of the images was corrected with an algorithm able to perform an ellipse fitting from an automatic determination of the planetary limb pixels (Ogohara et al. 2012, 2017). This automated identification of the limb becomes rather uncertain in many of the IR2 nightside images because of the light contamination previously described and also due to the frequent darkening of the planetary limb because of the strong variability of the clouds' opacity at lower latitudes (McGouldrick et al. 2008; Satoh et al. 2017). Instead, we coded an interactive tool inspired by the software WinJupos (Hahn & Jacquesson 2012) which allows the interactive adjustment of the position, size, and orientation of the planet's grid,¹⁵ using as reference four locations

on the limb chosen by the user (see Figure 2). The visualization of the limb was improved by interactively modifying the brightness and contrast in each image. In the case of the IR2 images, the position of the grid was adjusted with a precision of 1/10th of a pixel; its size was increased in some cases (less than 1.3% in all cases), while the orientation of the grid required no corrections. Regarding the ground-based images from NICS and SpeX, these were navigated using NASA's SPICE kernels (Acton 1996; Folkner et al. 2009); both the position and orientation of the grid were adjusted, and the predicted size was accurate enough to require no further corrections.

2.3. Techniques for Cloud Tracking

After correcting the navigation and processing the images, these were geometrically projected onto an equirectangular (cylindrical) geometry with an angular resolution similar to the best resolution in the original images. In those cases where the nightside images were acquired when *Akatsuki* was closer to its pericenter, the better spatial resolution enabled the wind speeds to be measured at polar latitudes, and azimuthal equidistant (polar) projections were performed too using an angular resolution similar to that found at latitudes of about 70° in the original image. Figure 3 shows examples of the original observations, their navigation after corrections, and cylindrical and polar maps. To measure the wind speeds, two different techniques of cloud tracking were employed: (a) a manual method applied to the full data set of IR2 and ground-based images (see Table 1), consisting of a manual search of the

¹⁵ The corrected geometry files are available from the corresponding author upon reasonable request.

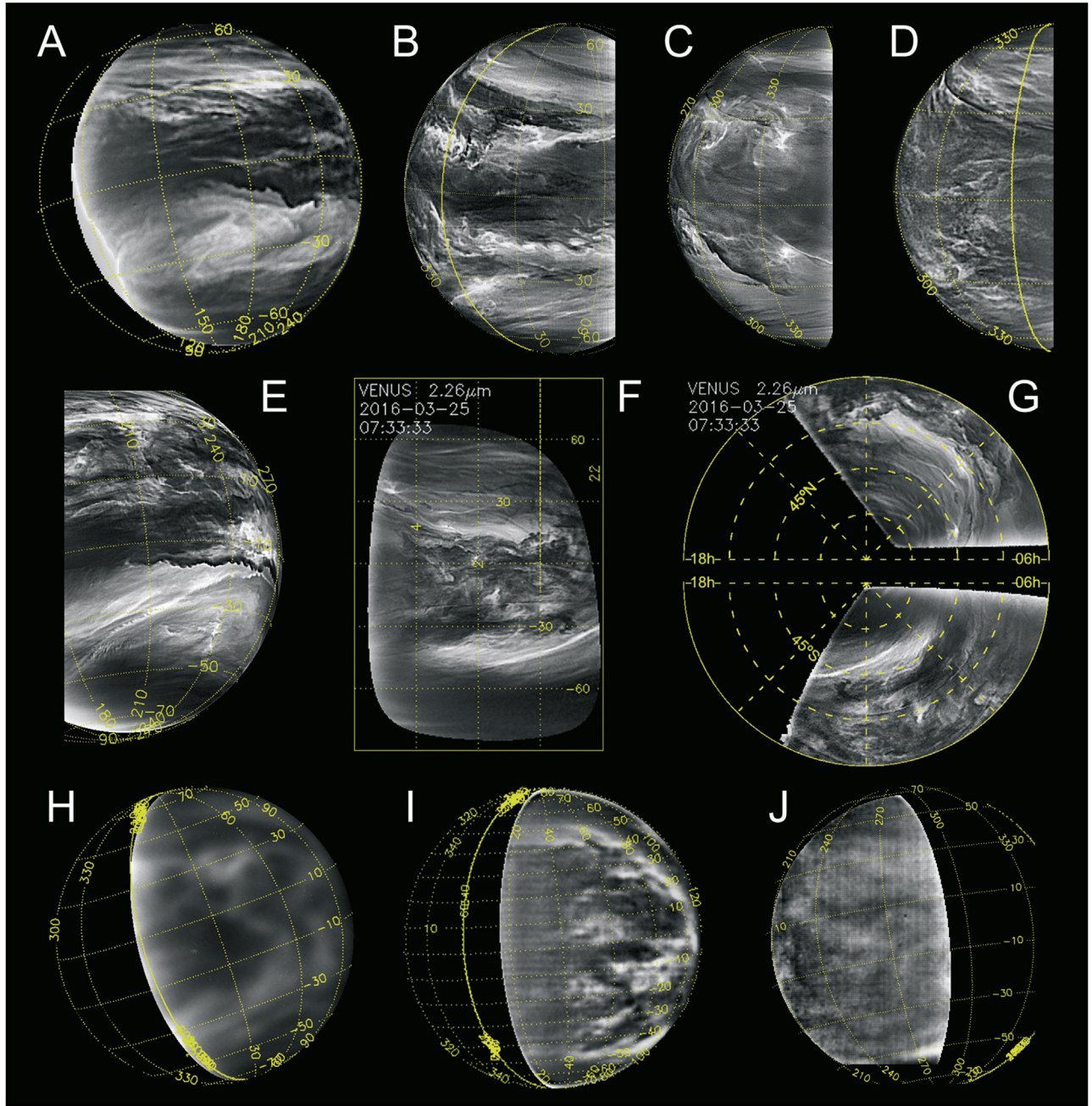


Figure 3. Examples of images acquired with the $2.26\ \mu\text{m}$ filter of *Akatsuki*/IR2 during the year 2016 (A–G) and ground-based observations at $2.32\ \mu\text{m}$ from TNG/NICS and IRTF/SpeX (H–J): (A) 2016 October 10, 09:23 UT, (B) 2016 August 13, 00:33 UT, (C) 2016 July 11, 22:03 UT, (D) 2016 July 22, 14:33 UT, (E) 2016 October 19, 14:33 UT, (F) cylindrical and (G) polar projections for 2016 March 25, 07:33 UT (original shown in Figure 6(A)), (H) 2012 July 11, 05:19 UT by TNG/NICS, (I) 2015 September 28, 16:03 UT by IRTF/SpeX, and (J) 2017 February 10, 02:31 UT by IRTF/SpeX. In the case of the polar projection (G), the northern and southern hemispheres are displayed above and below, respectively, with the geographical north/south poles located in the center.

cloud tracer followed by a fine adjustment using automatic template matching, which is visually accepted or rejected by a human operator (similar to that performed by Hueso et al. 2015); and (b) a fully automatic method used for images taken in 2016 July and August (see Table 1) and which uses the relaxation labeling technique (Ikegawa & Horinouchi 2016; Horinouchi et al. 2017b).

Wind measurements are obtained by comparing the position on the map of cloud features that can be identified in two consecutive images with a given time difference. We obtained wind measurements using a manual method in which we perform

automatic template matching with a phase-correlation technique that has also been applied for cloud tracking on Earth (Leese et al. 1970; Jun & Fengxian 1992; Humblot et al. 2005; Huang et al. 2012). We call this technique manual because a human user selects a region in the first image to obtain its best match in the second image and validates (or not) the final result. The phase correlation permits the translation between two images shifted relative to each other to be obtained (Kuglin 1975; Samritjarapon & Chitsobhuk 2008), relying on a frequency-domain representation of the images calculated with the Fast Fourier Transform (FFT) that enables this shift from the location of a peak to be

Table 1.
Coverage of the *Akatsuki*/IR2 Winds During the Year 2016

Month	Dates ^a	Latitudes	Local Times	Longitudes	Wind Vectors ^b
Mar	22, 23, 25–30	61°N–60°S	23–05 hr	225°–308°	249
Apr	15	43°N–63°S	01–06 hr	281°–348°	35+ 306
Jun	20	40°N–21°N	18–20 hr	264°–289°	12
Jul	1, 11 , 12, 22	72°N–69°S	18–01 hr	250°–23°	308+ 6920
Aug	2 , 9, 10 , 13 , 15–17 , 18, 19, 20 , 21, 22, 25 , 26 , 27, 28, 29 , 30	58°N–58°S	18–03 hr	322°–129°	1057+ 94656
Sep	4–6, 15, 26, 27	59°N–60°S	19–05 hr	28°–188°	347
Oct	2–7, 10–17, 19–27, 31	56°N–72°S	20–05 hr	114°–270°	939

Notes.

^a Bold characters stand for dates with wind measurements from both manual and fully automatic methods. Normal characters are used for dates with only manual measurements.

^b Normal and bold characters stand for number of wind measurements obtained with the manual and fully automatic methods, respectively.

inferred in a cross-correlogram. Figure 4 shows an example of the use of this technique where the narrow peak in the phase cross-correlogram is shown for a well-identified tracer. A more complete explanation about the phase correlation is provided by Kuglin (1976). Compared to the standard correlation, its performance is faster, and it is less sensitive to random noise and illumination conditions (Ahmed & Jafri 2008). Even though the phase correlation can potentially register subpixel displacements (Reddy & Chatterji 1996; Foroosh et al. 2002), we did not test this capability in this work and only accounted for displacements expressed as integers of pixels. Besides, since the boundaries of any image imply discontinuities in the signal that can introduce a noisier result, zero padding is advisable before applying the FFT (Ahmed & Jafri 2008). For this reason, the initial and final templates (ranging in sizes of 32×32 to 48×48 pixels) were convolved with a Hanning window with a width of 0.7 before the FFT was applied. When no clear peak could be found with the phase correlation, or when the tracer identification was judged as not satisfactory by the human operator running the analysis, the wind measurement was rejected and the template matching was performed manually. Each of these manual measurements was verified by a human operator looking at visual reports such as the one shown in Figure 4.

A fully automatic technique based on classical image correlation for identifying the cloud tracers' motions was also used by Horinouchi et al. (2017a, 2017b), and we will show here a detailed report of these measurements. This technique is similar to that used in many previous studies of Venus cloud dynamics (Rossow et al. 1990; Kouyama et al. 2012; Khatuntsev et al. 2017; Horinouchi et al. 2018), but in this case, the cross-correlation between images is computed along a sequence of images to estimate the horizontal velocity at a specific location (Horinouchi et al. 2017a, see the Methods section therein). This method was applied to images of the lower clouds acquired in 2.26 and $1.74 \mu\text{m}$. All of the IR2 images were projected onto an equirectangular geometry with a fixed angular resolution of 0.125° per pixel regardless of the resolution of the original images (Ogohara et al. 2017). Image processing was applied after the projection and consisted of a two-dimensional bandpass filter with Gaussian functions with sigma values of 0.25° for the low pass filter and 3° for the high pass filter with latitude and longitude. Finally, the template size

for cloud tracking was set to a fixed value of 60×60 pixels for all images.

3. Meridional Profiles of Wind Speeds

A total of 2947 wind vectors were obtained with the manual method for the nightside images of the IR2 camera for the full period covering 2016 March 22 (when pairs of IR2 images were taken within the same day for the first time) until October 31. The spatial resolution of the images ranged from 10 to 80 km per pixel, and we selected pairs of images with time separations ranging from 1 hr up to 22 hr (for special cases of clouds displaying very small deformations over large time-scales). The size of the cloud tracers comprise dimensions ranging from 510 to 2550 km, depending on the spatial resolution selected for the geometrical projections. Images acquired over 2016 April, July, and August were also independently measured with the fully automatic method described above, resulting in 149,033 wind measurements from the tracking of cloud features with a fixed size of 790 km. The errors for the wind speeds obtained with manual tracking were calculated from the spatial resolution and the time interval between the images as explained by Bevington & Robinson (1992), while in the case of automatic cloud tracking, the calculation of errors is explained by Ikegawa & Horinouchi (2016).

Satoh et al. (2017, Figure 11(b) therein) and Limaye et al. (2018, Figure 15 therein) show *Akatsuki* IR2 images of strong cloud discontinuities in the lower clouds of Venus. These discontinuities propagate faster than the background zonal flow and were suspected to be the manifestation of waves rather than passive tracers. For this reason, we discarded the motions of these strong opacity discontinuities from our study of global wind motions. In the case of automatic cloud tracking, we ruled out all measurements obtained from image pairs where this equatorial cloud discontinuity was apparent. As a result of this filtering, the number of wind vectors from the manual and automatic methods was reduced to 2277 and 101,882, respectively. Since the automatic method does not provide a registry of the cloud morphologies tracked, this filtering also removed all automatically generated wind vectors during 2016 April. Table 1 summarizes the results obtained with both techniques in different time periods and their coverage over the

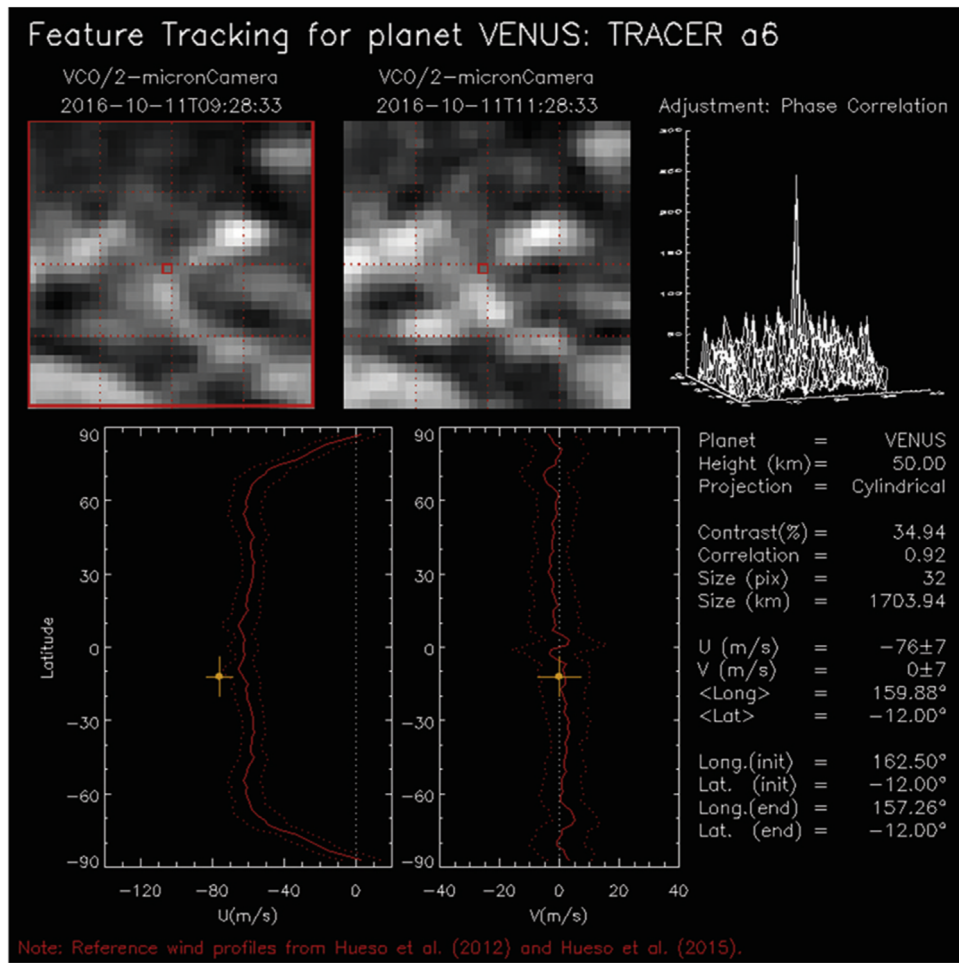


Figure 4. Example of positive identification of a cloud tracer in a pair of IR2 images using phase correlation. Note that when a match is successful (see templates), a single and clear peak—ideally a Kronecker delta—is apparent in the cross-correlogram located in the upper-right corner. The inferred wind speeds are compared with a reference wind profile from VEx/VIRTIS-M (Hueso et al. 2012) in the two graphs below, while detailed information is provided on the right side, below the correlogram. A complete report of the clouds’ matches using phase correlation can be found in the supplemental material (see the [Appendix](#)).

planet. The full report of wind measurements from the $2.26 \mu\text{m}$ IR2 images without specific features filtered out and obtained with the manual method can be found in the supplemental material (see the [Appendix](#)), which includes a table with the complete data set of wind measurements with manual tracking, geometrical projections, animations, and detailed template-matching results.

3.1. Morphologies of the Nightside Clouds

Panels (A)–(G) in Figure 3 exhibit a sample of the clouds’ morphologies observed in the IR2/ $2.26 \mu\text{m}$ images. Pioneering ground-based observations at these wavelengths (Allen & Crawford 1984; Crisp et al. 1991) show global characteristics similar to those of the *Akatsuki* IR2 images. The deeper clouds on the nightside of Venus are normally characterized by a dark band with high-opacity clouds at low latitudes, while the midlatitudes are dominated by brighter bands with lower opacity (see Figures 3(A)–(B)). Prior to *Akatsuki*, the midlatitude bands appeared almost featureless (Crisp et al. 1991; Limaye et al. 2006; Hueso et al. 2012). However, the higher spatial resolution of the *Akatsuki* IR2 images reveals subtle though distinguishable wisps and patches (Figures 3(F)–(G)) on them,

sometimes invaded by broad bands of clouds with higher opacity (Figure 3(B)) or unusual sharp dark spirals tilted relative to the latitude parallels (Figures 3(C)–(D)), which spread thousands of kilometers from latitudes higher than 30° toward equatorial ones (Horinouchi et al. 2017a; Satoh et al. 2017; Limaye et al. 2018).

In the IR2 images, the clouds’ opacity exhibits higher variability at lower latitudes than at midlatitudes (Satoh et al. 2017; Limaye et al. 2018), confirming previous findings with ground-based observations (Crisp et al. 1991; Limaye et al. 2006; Tavenner et al. 2008; Mota Machado et al. 2016) and during the VEx mission (Hueso et al. 2012; McGouldrick et al. 2012; McGouldrick & Tsang 2017). Dark areas of high opacity normally dominate at lower latitudes, while their boundary with the midlatitude bright bands exhibits complex cloud features (Horinouchi et al. 2017a; Limaye et al. 2018), like small vortices or abundant bright swirls at around 30° , which sometimes adopt shapes suggestive of shear instabilities (Figures 3(B), (C), and (E)), similar to those found at the nightside upper clouds at $\sim 65 \text{ km}$ in the $3.8 \mu\text{m}$ VEx images (Peralta et al. 2017a). The polar projection in Figure 3(G) clearly exhibits an example of the frequent episodes of hemispherical asymmetry of the morphology of the Venus clouds. A more

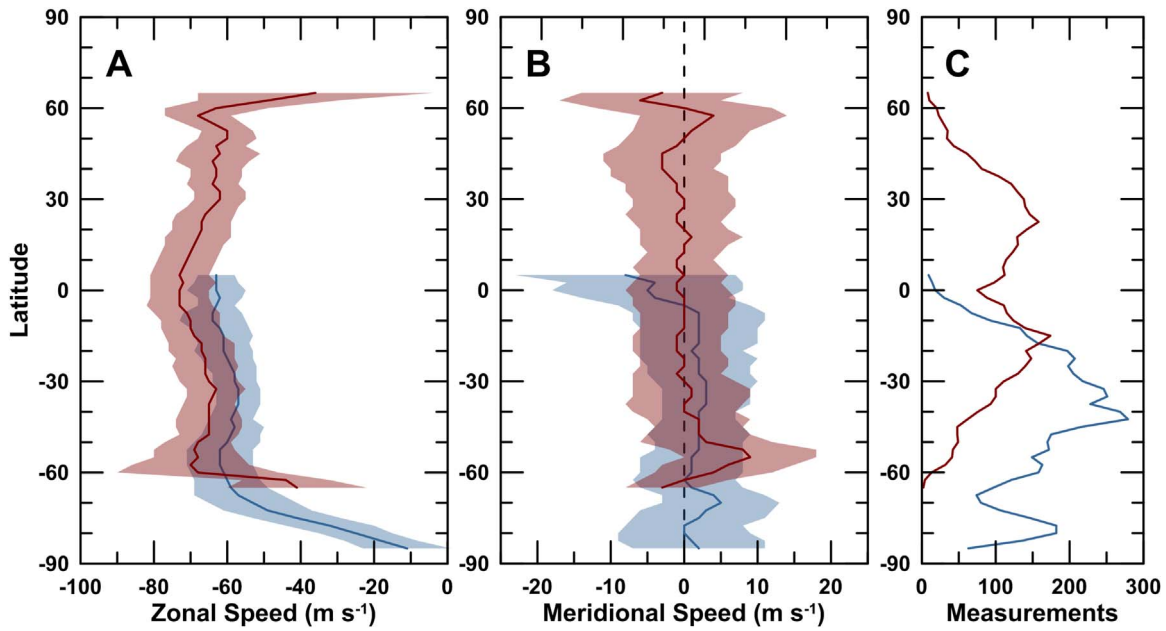


Figure 5. Mean profiles of the winds at the nightside middle to lower clouds of Venus as measured from 2016 March to October with the manual method from the *Akatsuki*/IR2 2.26 μm images (dark red line). These profiles are compared with the winds measured from the 1.74 μm images acquired with *VEx*/VIRTIS-M (blue line) between 2006 April and 2008 August (Hueso et al. 2012). The profiles for the zonal and meridional components are shown in panels (A) and (B), respectively. The average values shown here were calculated for bins of 5° latitude, and the number of measurements used in each bin is displayed in panel (C). The shaded areas stand for the standard deviation at every latitude bin when this is larger than the measurement error computed from the image resolution and time differences in the image pair.

complete survey of the clouds’ morphologies apparent in the images from the *Akatsuki*/IR2 camera will be presented elsewhere.

3.2. Latitudinal Profiles of the Winds and Relation with Clouds

Figure 5 shows zonally averaged profiles of the manually tracked winds at the lower clouds during the first year of *Akatsuki* observations. Bins of 5° latitude were considered to calculate the average wind speeds from 2016 March to October. The profiles of IR2 are compared with the *VEx*/VIRTIS-M results from 2006 April to 2008 August (Hueso et al. 2012). With regard to the zonal component of the wind (Figure 5(A)), the mean profile obtained with IR2 is faster than the VIRTIS-M measurements by 10 m s^{-1} . The zonal winds from IR2 observations show symmetric profiles between both hemispheres and, despite the higher dispersion at higher latitudes, due to the poorer spatial resolution of the IR2 images close to the poles, they show for the first time the decay of the winds toward the poles on both hemispheres simultaneously. This decay starts at about 60° and, compared to the *VEx* results, it seems more abrupt, although it retains similarities with the wind profiles obtained in 2004 with ground-based observations (Limaye et al. 2006, Figure 5 therein), albeit with higher errors. However, we cannot rule out that these differences at subpolar latitudes with respect to the *VEx*/VIRTIS-M subpolar winds are not caused by the worse spatial resolution at polar latitudes and the low number of measurements in the *Akatsuki* IR2 images (Figure 5(C)). Regarding the meridional component of the wind (Figure 5(B)), the results from 2016 and 2006–2008 are in good agreement, confirming the absence of clear global motions in the meridional circulation of the nightside lower clouds.

Wind variability is also apparent during 2016 (see Figure 6). The profile obtained on 2016 March 25 (Figure 6(A))

corresponds to winds that are approximately constant between the equator and midlatitudes with small meridional shear. This seems to be the most frequent case found at the lower clouds during the *Akatsuki* observations and also during the *VEx* mission (Hueso et al. 2012, Figure 17 therein). Zonal wind profiles on other dates, such as July 11 (Figures 6(B)) and October 13 (6(C)), exhibit more intense equatorial zonal speeds, reported for the first time during the *Galileo* flyby (Crisp et al. 1991, Figure 4 therein) and later identified as recurrent episodes of jets at the equator (Horinouchi et al. 2017a). There is a reasonable correspondence between this local intensification of zonal speeds and the presence of features resembling shear instabilities (Figure 6(B)) or sharp opacity discontinuities at the equator (Figure 6(C)). The high dispersion in the horizontal speeds also suggests that these jets may be apparent only in a rather longitudinally narrow area. The profile during July 11 (Figure 6(B)) shows that these jets can sometimes show up at northern latitudes, as also reported in 1990 during the *Galileo* flyby (Carlson et al. 1991, Figure 6 therein) and in 1996 from observations at the Apache Point Observatory (Chanover et al. 1998, Figure 7 therein).

4. Sources of Variability for the Wind Speeds at the Lower Clouds

In this section, we explore whether the size of the features tracked, the opacity of the clouds, the uncertainties in their vertical sensing, or a dependence on the local time and surface elevations can help explain the variability observed in the winds of the nightside lower clouds.

4.1. Effect of the Opacity and Size of the Clouds

It is still unclear whether the episodes of faster zonal speeds shown in Figure 6 are related to horizontal and/or vertical

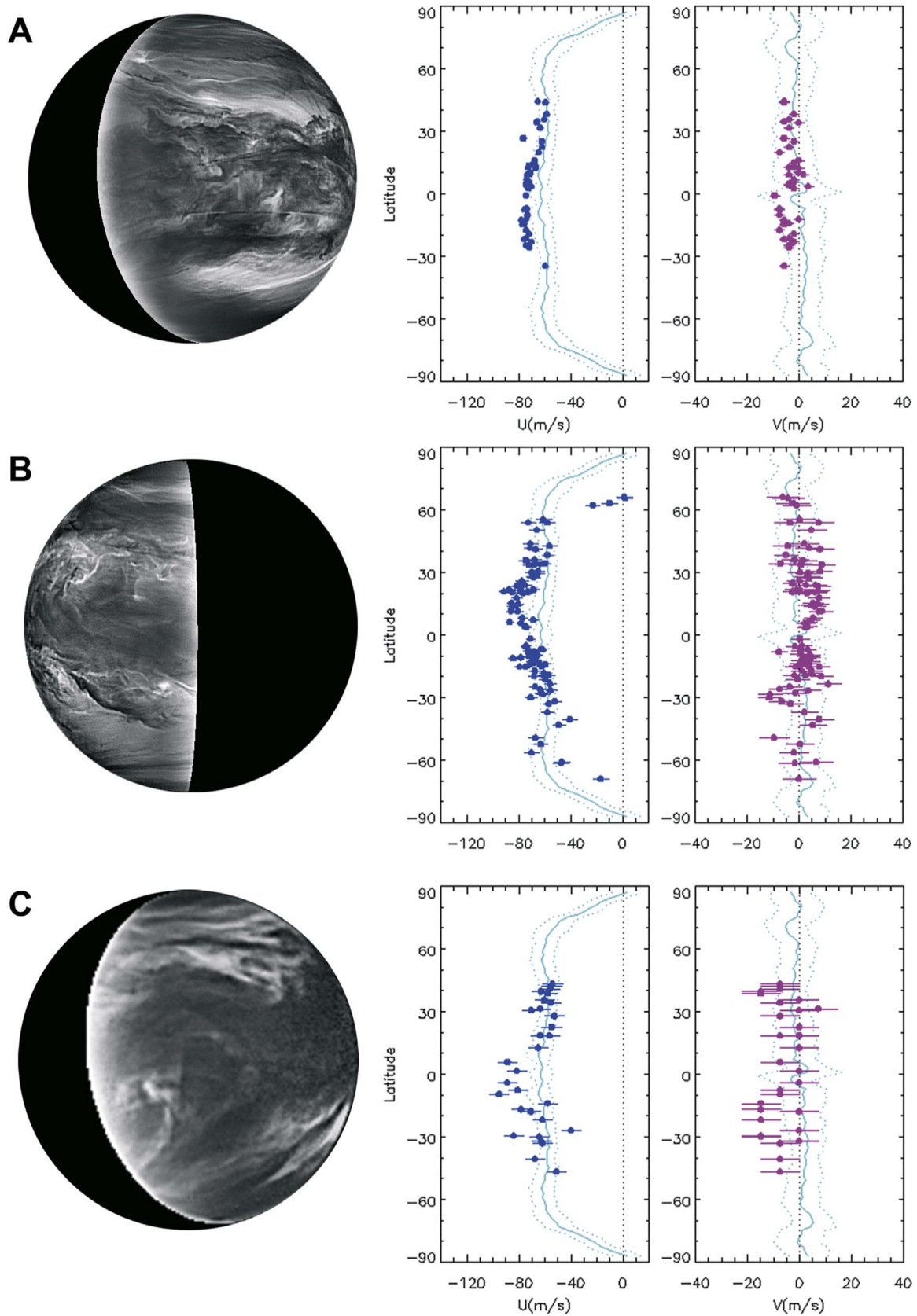


Figure 6. Variability in the clouds' morphology (left column) and profiles of zonal and meridional winds (center and right columns) during the *Akatsuki* mission in 2016: (A) winds during March 25, exhibiting the standard profile of constant zonal speeds, (B) winds during July 11, displaying a zonal jet at $\sim 20^\circ\text{N}$, and (C) winds during October 13, exhibiting a strong jet at the equator and higher dispersion in the southern hemisphere. Reference profiles built from winds during the *VEx* mission (Hueso et al. 2012) and plotted in a symmetric way for the two hemispheres are displayed in cyan.

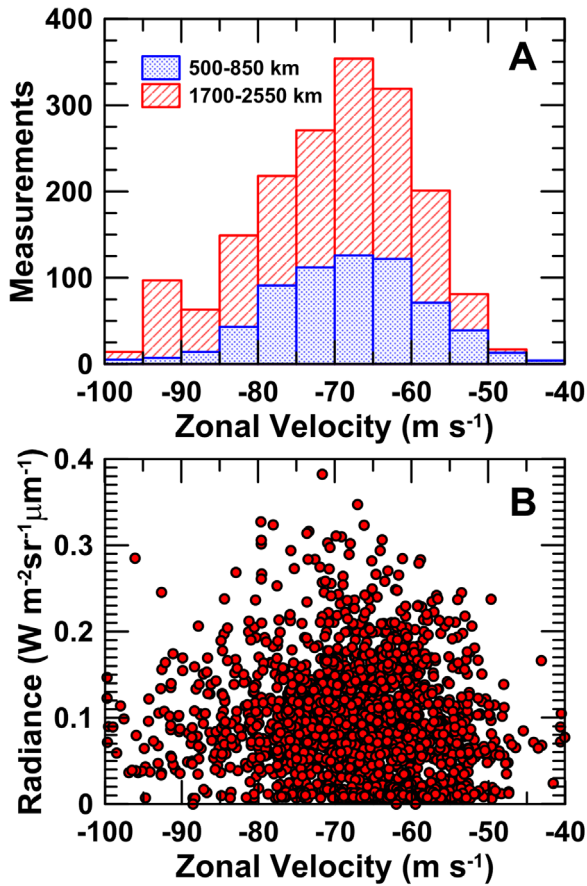


Figure 7. Histograms and scatter plot of the wind measurements acquired with the manual method and *Akatsuki*/IR2 images. Panel (A) shows the histograms of the zonal velocities for two ranges of spatial scales of cloud tracers. Panel (B) exhibits the values of zonal wind speeds in terms of the mean radiance (red dots). The radiance is given for the calibration version “v20170601” of the IR2 2.26 μm images and corresponds to the radiance average inside the template.

gradients of the zonal wind, or if the bright and dark clouds observed on the nightside at 1.74, 2.26, and 2.32 μm are moving at the same or at slightly different vertical levels. Early interpretations of Venus IR features considered that these clouds’ contrasts might be caused either by scattered sunlight leaking in from the dayside along altitudes with low absorption in the CO_2 windows, or that the dark areas corresponded to opaque clouds lying in a broken layer at a certain altitude above the brighter regions and radiate as blackbodies at the lower temperature of their tops (Allen & Crawford 1984). Allen (1987) discarded both interpretations, confirming that the existence of important differences in the vertical elevation of bright and dark clouds was inconsistent with the small variations that the dark/bright areas exhibit in CO absorptions affecting the wide 2.2–2.3 μm band. Therefore, the dark and bright regions should correspond to horizontal inhomogeneities in the clouds’ opacity to deeper background thermal emission (Allen 1987; Crisp et al. 1989), although certain discrepancies in the altitude between dark and bright clouds cannot be disregarded, since these inhomogeneities can be caused by variations in the size and distribution of the particles within the lower and middle clouds (McGouldrick & Toon 2008).

Assuming a range of 50 to 60 km for the altitudes sensed at the relevant wavelengths (McGouldrick et al. 2008), a

comparison with in situ wind profiles from descending probes (Counselman et al. 1980; Gierasch et al. 1997; Moroz & Zasova 1997) indicates that variations of up to 30 m s^{-1} could be explained in terms of the vertical shear (Peralta et al. 2017a, Figure 3 therein), which is also consistent with the magnitude of the reported jets (Horinouchi et al. 2017a, Figure 2(b) therein). Crisp et al. (1991) obtained a discrepancy between the velocities of large dark clouds and the smaller markings (sizes ranging from 400 to 1000 km), and also suggested that these might be produced at different altitudes. Figure 7 displays the distribution of zonal speeds obtained with the manual method compared with the average radiance (Figure 7(B)) and the size of the cloud tracers between 50°N and 50°S (Figure 7(A)) in the IR2 2.26 μm images. No dependence is apparent between the zonal velocities and these parameters. Since the low latitudes frequently exhibit cloud patterns that resemble shear instabilities for a wide range of scales (see Figures 3(C)–(E); Limaye et al. 2018, Figure 10 therein), the generation of jets due to meridional gradients in the horizontal winds seems probable. McGouldrick & Toon (2007, 2008) showed that large-scale dynamics can also explain the strong variations in the cloud opacity, and that even weak downwelling is able to produce optical-depth holes in the clouds.

4.2. Local Time Dependence

Since most of the sunlight absorption on Venus occurs within the clouds’ layer, solar tides are expected to be excited and carry momentum upwards and downwards away from the region of excitation, thus accelerating the atmosphere westwards and contributing to the RZS (Gierasch et al. 1997; Sánchez-Lavega et al. 2017). The effect of solar tides has been unambiguously detected on both zonal and meridional components of the winds at the upper clouds at 65–70 km (Rossow et al. 1990; Limaye 2007; Sánchez-Lavega et al. 2008; Kouyama et al. 2012; Peralta et al. 2012; Khatuntsev et al. 2013; Hueso et al. 2015), but no evident influence has been found for the middle to lower clouds (50–60 km) for either day (Hueso et al. 2015; Khatuntsev et al. 2017) or night (Hueso et al. 2012, Figure 6 therein). Khatuntsev et al. (2017) argued that this negligible effect of the solar tides could be related to the absence of an unknown absorber downward of the middle clouds (which is responsible for most of the solar heat deposition on Venus).

Figure 8 allows the local time dependence for the winds at the nightside lower clouds of Venus during 2016 to be studied. In agreement with *VEx* during 2006–2008, no local time dependence is apparent in the meridional winds (Figure 8(B)). However, the zonal component of the wind speed displays a local increase of the zonal speeds between 19 and 22 LT, followed by a gradual decrease toward late nightside local times (a decrease of $\sim 10 \text{ m s}^{-1}$ between 19 LT and midnight). Hueso et al. (2012) also reported hints of faster retrograde winds close to dawn during 2006–2008, although this local time effect was weaker and disregarded due to the small number of measurements in this area. Recent results from Venus General Circulation Models (hereafter GCMs) predict that the diurnal tide should be also apparent on the zonal wind down to the middle clouds at $\sim 60 \text{ km}$ with the slowest speeds centered at the evening terminator (Takagi et al. 2018, Figure 3(a) therein). Better agreement is found for the GCM results at the lower

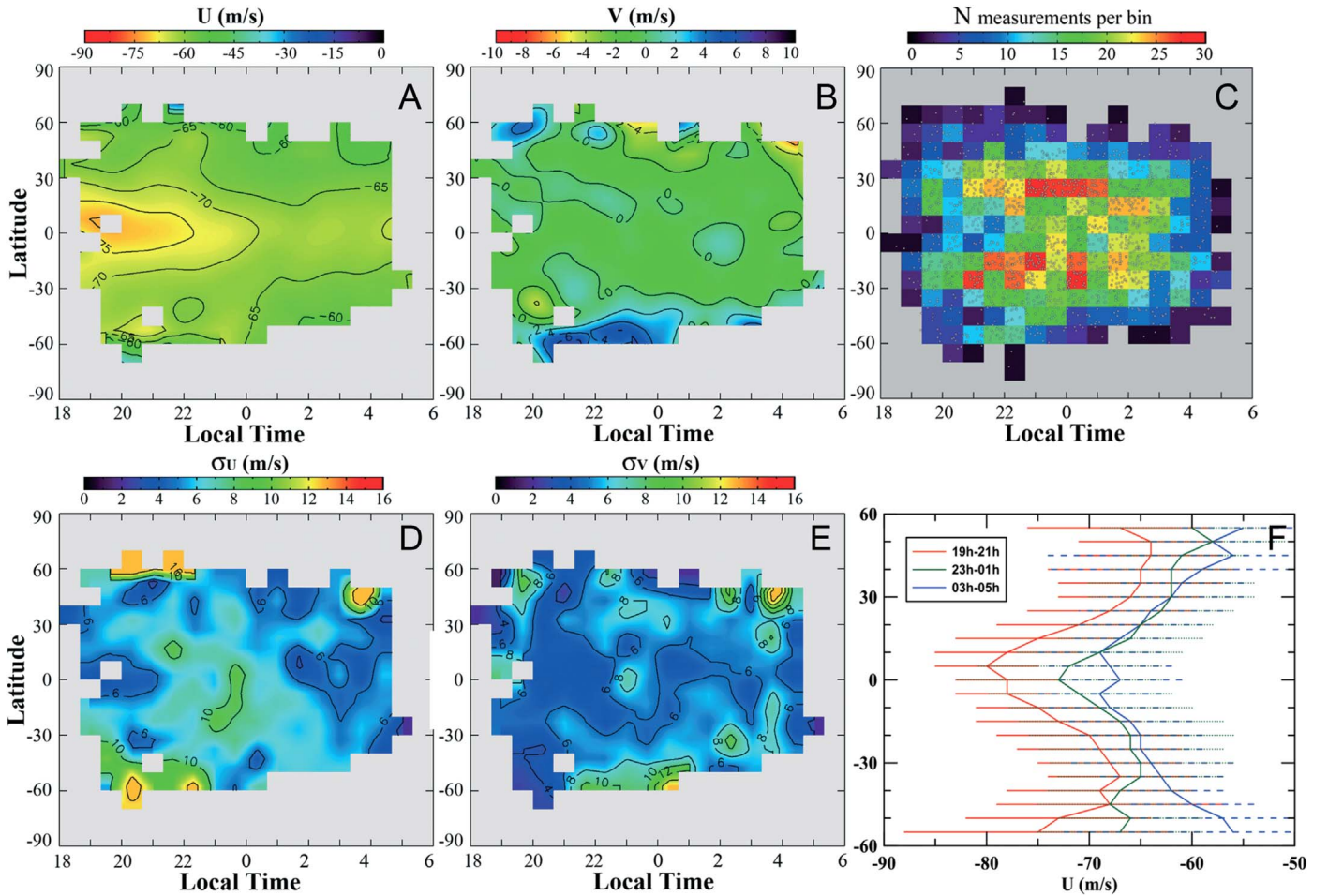


Figure 8. Local time dependence for the zonal winds obtained with the manual method from the *Akatsuki*/IR2 $2.26\ \mu\text{m}$ images. Bins of 10° in latitude and 40 minutes in local time were used. Panels (A) and (B) display the values of the zonal and meridional components of the wind averaged in each bin, panel (C) shows the distribution of wind measurements with dots representing individual measurements, panels (D) and (E) display the standard deviation of the measurements in each bin, and panel (F) shows the meridional profiles of the zonal winds at different intervals of local time.

clouds ($\sim 50\text{ km}$), where the influence of the diurnal tide is predicted to weaken but a local maximum of about 10 m s^{-1} is also found in the early night and before midnight (Takagi et al. 2018, Figure 4(a) therein).

4.3. Longitudinal Dependence

Evidences of how the surface topography may be influencing the atmospheric circulation through the excitation of atmospheric stationary waves (lee waves) have been accumulating. Vertical disturbances experienced by the VEGA-2 balloon over Aphrodite Terra (Blamont et al. 1986), strong asymmetries of the water vapor over certain geographical locations (Fedorova et al. 2016), and the finding of multiple stationary waves at the upper clouds of Venus, which are strongly correlated with the surface elevations (Fukuhara et al. 2017; Kouyama et al. 2017; Peralta et al. 2017a), strongly suggest surface effects on the upper atmosphere. Results of cloud tracking in the VEx/VMC dayside images seem to support the fact that the wind speeds at the cloud tops are decelerated as they pass over Aphrodite Terra and Atla Regio (Bertaux et al. 2016, Figures 4 and 6 therein). Other works have reported indications of an effect of surface elevations for the winds at the middle clouds

(Khatuntsev et al. 2017, Figure 14 therein) and over the oxygen airglow patterns (Gorinov et al. 2018). Peralta et al. (2017a) discovered that during 2006–2008, the RZS at the nightside upper clouds exhibited a higher variability compared to the dayside ones, but the geographical coverage of the wind measurements was insufficient to confirm a correlated effect with the surface elevations. In the case of the lower clouds on the nightside, stationary waves are paradoxically missing in the clouds’ opacity and no longitudinal dependence had been reported for the wind speeds (a reanalysis of VIRTIS-M winds for the lower clouds was inconclusive due to the lack of data to separate local time effects from time variability and the elusive surface dependence). Figure 9 displays the dependence on the longitude and latitude of the manual wind measurements with the *Akatsuki* IR2 images. While no clear effect is found for the meridional component of the wind (Figure 9(B)), the westward wind speeds exhibit a local maximum at low latitudes over the longitude range 300° – 120° (Figure 9(A)).

Unfortunately, separating the effects of the longitudinal and local time dependences is not feasible with our results, since the observed velocity disturbances are just marginally larger than the corresponding errors and the incomplete coverage of

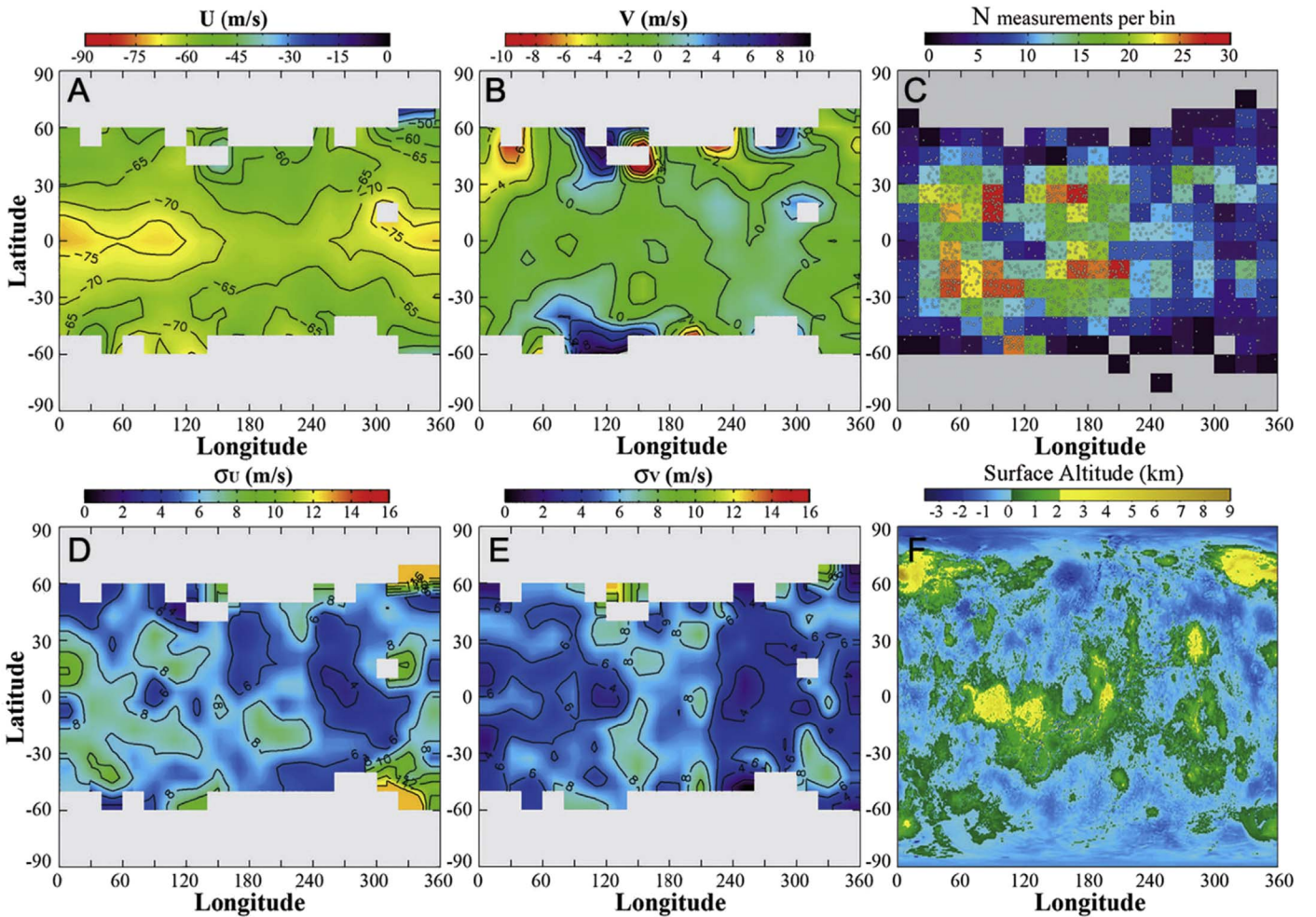


Figure 9. Local time dependence for the zonal winds obtained with the manual method on the *Akatsuki*/IR2 2.26 μm images. Bins of 10° and $40'$ were considered for the latitude and local time, respectively. Panels (A) and (B) display the values of the zonal and meridional components of the wind averaged in each bin, panel (C) shows the distribution of wind measurements, panels (D) and (E) display the error (standard deviation) in each bin, and panel (F) exhibits the surface elevation of Venus for comparison.

our wind measurements. Figure 10 shows the distribution of the mean zonal speeds (Figure 10(A)) and the number of measurements (Figure 10(B)) in terms of local time and longitude. To avoid the expected decrease of the zonal winds toward the poles, only the *Akatsuki*/IR2 wind measurements between 50°N and 50°S were considered. Figure 10(B) shows that the number of wind measurements during the year 2016 is irregularly distributed for both longitude and local time parameters, preventing a confirmation of either a local time dependence and/or influence of surface elevations.

However, the influence of the surface elevations on the zonal winds at the nightside lower clouds might still be regarded as controversial. Published results for the zonal winds on the dayside originated from a huge set of wind measurements with noticeable dispersion (Bertaux et al. 2016, Figure 2 therein), and authors do not report filtering out other important sources of variability such as transient waves or the local time dependence. In the case of zonal wind speeds obtained with the *Akatsuki*/UVI images, Horinouchi et al. (2018) characterized and removed the local time dependence on the zonal winds at the dayside upper clouds. As a result, no effect of surface elevations was found for the dayside winds (Horinouchi et al. 2018, Figure 14(b) therein).

In the case of our results for the nightside lower clouds, the local maximum extends mostly over rather plain areas and does not seem well correlated with the surface elevations at lower latitudes. Moreover, our results seem inconsistent with those on the dayside reported by Bertaux et al. (2016) and Khatuntsev et al. (2017) since, opposite to the zonal wind speeds on the dayside from VEx/VMC, which exhibit a local minimum with slower speeds extending along 0° to 200° (Bertaux et al. 2016, Figure 3 therein), our westward winds on the nightside display a local maximum between longitudes 300° and 120° .

4.4. Results from Automatically Retrieved Winds during 2016 July and August

We now explore possible wind dependencies on the factors shown above for our wind results obtained with the automatic cloud correlation technique and first reported by Horinouchi et al. (2017a). The dependence on both local time and longitude for the winds obtained with the fully automatic method is displayed in Figure 11. Since for these wind speeds only IR2 images obtained during 2016 July and August were used (see Table 1), the coverage is more limited than in the case of the

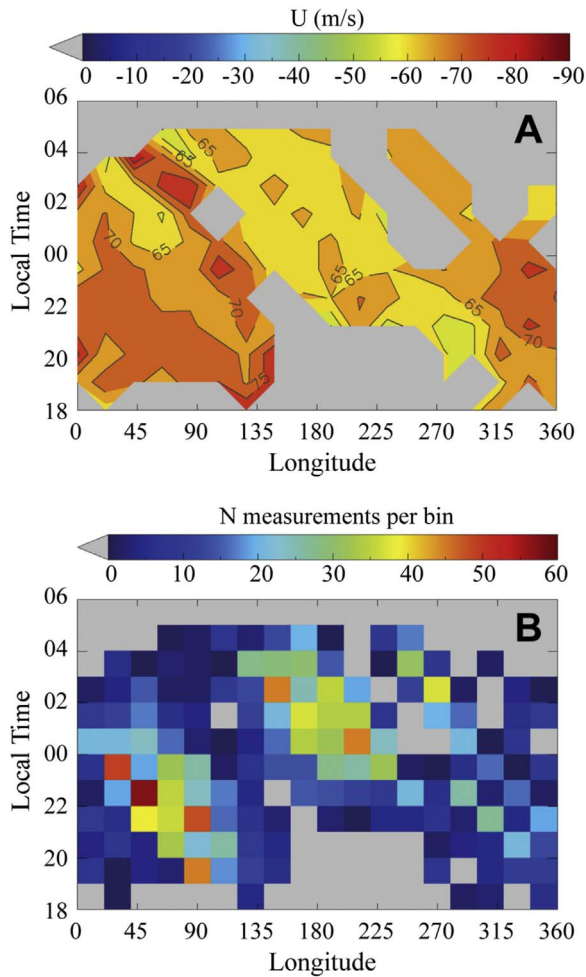


Figure 10. Distribution of the wind measurements acquired with the manual method and *Akatsuki*/IR2 images between 50°N and 50°S as a function of longitude and local time. Panel (A) displays the distribution of the zonal wind speeds. Panel (B) shows the distribution of the number of measurements.

manual method, and the dispersion is smaller than for the manual results (see Figures 8(D), (E), 9(D), and (E)).

Except for the case of the meridional winds where no clear dependence on the local time and longitude is found, the zonal winds with automatic correlation are not fully consistent with those from manual wind measurements, and no influence over the zonal speeds is observed at any range of local time or longitude. Even though some discrepancies were expected between both cloud tracking methods and the different techniques to correct the navigation of the IR2 images, the homogeneity found for the zonal winds at low latitudes might be explained by the recurrence of the equatorial jet during 2016 August (Horinouchi et al. 2017a), which would mask a weaker dependence on local time and/or longitude.

4.5. Combined Results of *Akatsuki* and Venus Express

We also combined the wind speeds at the nightside lower clouds from *Akatsuki*/IR2 in the year 2016 using the manual method with those obtained by Hueso et al. (2012) from *VEx*/VIRTIS-M from 2006 to 2008. Since the mean zonal winds during 2016 were faster than those during the *VEx* mission (see

Figure 5(A)), the difference between the zonal averages of both data sets equatorward of the midlatitudes was suppressed by multiplying by a correcting factor of 1.06 the zonal speeds obtained from the *VEx*/VIRTIS-M images, while those from the *Akatsuki*/IR2 images were divided by 1.06. As a result, a correction of $\sim 4 \text{ m s}^{-1}$ was introduced in both sets of winds. Also, these two data sets have a comparable number of points, and both are based on cloud tracking inspected/validated by human operators. The result of their combination is presented in Figure 12. The dependence on the local time (Figures 12(A)–(B) and (E)–(F)) confirms the equatorial maximum of the zonal speeds between local hours 18–22 hr, while this dependence clearly decays toward higher latitudes. On the other hand, the meridional component of the wind displays no apparent dependence at low latitudes, while at the higher latitudes of the southern hemisphere (50°S–90°S) and between 21 and 22 hr, it exhibits an equatorward acceleration (Figure 12(B)). These results, again, suggest that the solar tide detected in the winds of the upper clouds (Limaye 2007; Peralta et al. 2012) might be able to propagate downwards to the middle clouds as predicted by some Venus GCMs (Takagi et al. 2018). Regarding the dependence on longitude and surface elevations, the local maximum between longitudes 300°–120° reported in Section 4.3 for the westward wind speeds is observed (Figure 12(C)), while the meridional component exhibits no clear influence of the surface elevation (Figure 12(D)).

5. Time Evolution of the Winds

Results from past space missions to Venus and comparison among them have provided evidence of long-term variability affecting the atmospheric dynamics at the upper clouds of Venus (Sánchez-Lavega et al. 2017, Figure 2 therein). Rossow et al. (1990) reported that during the *Pioneer* Venus mission, Venus zonal winds at the equator and midlatitudes exhibited variations ranging from 5 to 8 m s^{-1} over time spanning one to six years, while the intensity of the poleward circulation seemed also subject to variability. From the analysis of the ultraviolet albedo of the cloud tops in different missions, del Genio & Rossow (1990) suggested that between 1979 and 1986, the clouds' dynamics might have experienced cyclic changes with a timescale of 5–10 years. This conclusion was based on periods of the presence/absence of four- and five-day wave modes, while during the *VEx* mission, Lee et al. (2015a, Figure 18 therein) reported unexplained periods of 154, 275, 357, and 560 days on the 365 nm albedo.

Long-term trends were also observed for the dayside winds of the upper clouds during the *VEx* mission. Between 2006 and 2013, the mean zonal velocity measured from the ultraviolet images from the VMC camera displayed an increase from 80 to 100 m s^{-1} at about 20°S (Khatuntsev et al. 2013, Figure 14 therein), while a similar increasing trend was independently confirmed in this period with cloud tracking in the VIRTIS-M images (Hueso et al. 2015). Kouyama et al. (2013) analyzed the *VEx*/VMC images, finding that the zonal winds equatorward of 30°S exhibited a periodical perturbation of $\sim 10 \text{ m s}^{-1}$ every 257 ± 2 terrestrial days, which was ultimately interpreted as centrifugal waves (Peralta et al. 2014, Figure 4 therein). Measurements with the *Akatsuki*/UVI images have also confirmed zonal wind speed variations with timescales of ~ 100 days between 2015

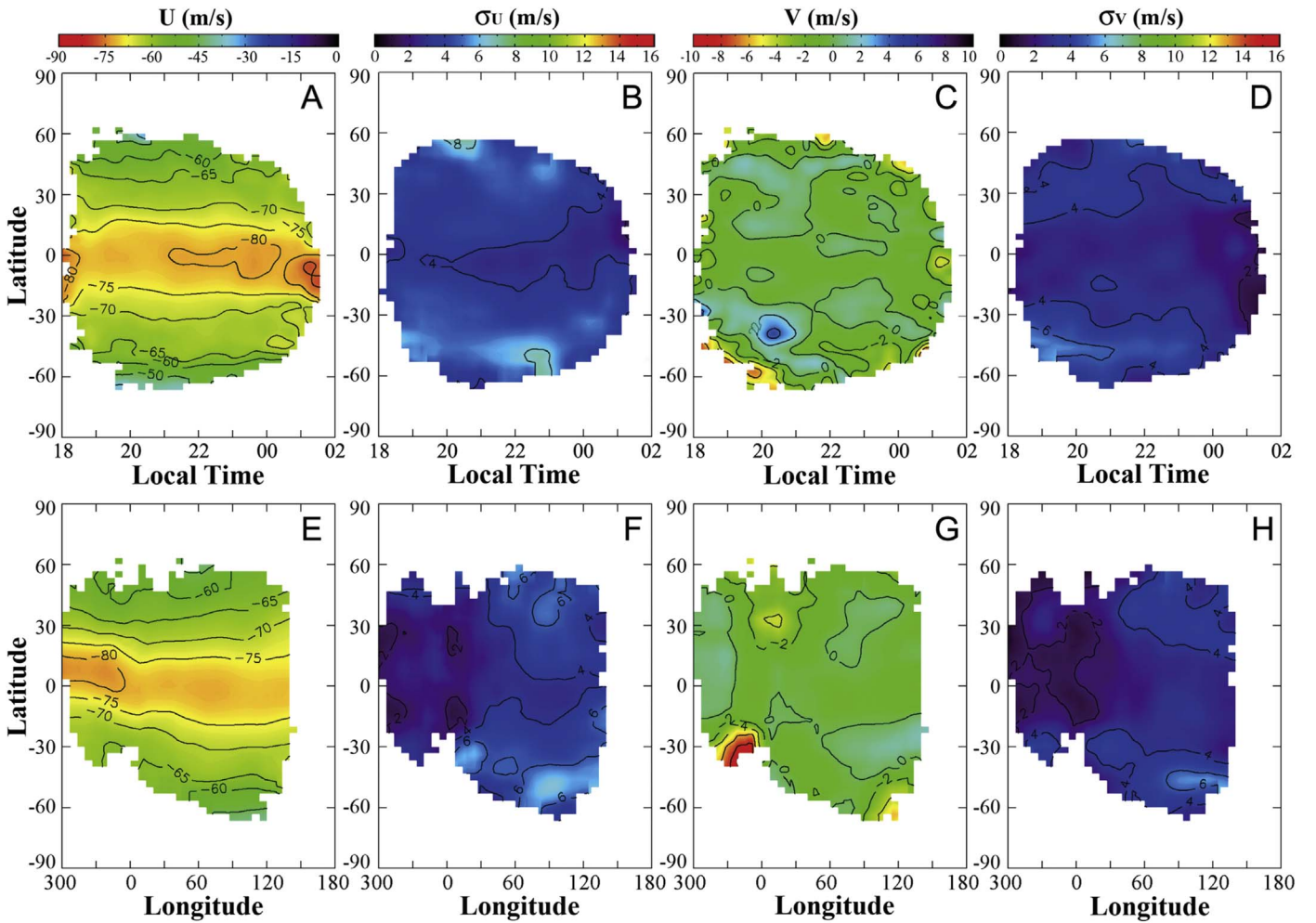


Figure 11. Contour maps for the dependence of the zonal and meridional winds obtained with the fully automatic method from the *Akatsuki*/IR2 images. Averages are given in panels A, C, E, and G, and standard deviation in panels B, D, F, and H. The larger number of wind measurements allows these maps to be calculated with bins of latitude, longitude, and local time of 3° , 3° , and 13 minutes, respectively, or three times smaller than those in the manual tracking results. However, the spatial coverage over local times and longitudes is more limited in this case due to the data coming from a smaller number of dates.

December and 2017 March (Horinouchi et al. 2018, Figures 8–10 therein). Numerical simulations with GCMs have also been used to predict decadal variation in the zonal winds in Venus (Parish et al. 2011).

The long-term variability of the winds at the level of the lower clouds was studied during the *VEx* mission on the nightside with VIRTIS-M by Hueso et al. (2012) and on the dayside with VMC by Khatuntsev et al. (2017). During the years 2006 to 2008, the nightside winds at the deeper clouds showed stronger variability at subpolar latitudes than at lower ones (Hueso et al. 2012, Figures 7–8 therein), while a comparison between the zonal winds during the *Galileo* flyby in 1990 and the two-year average from *VEx* does not indicate noticeable variations except for the northern jet reported from the *Galileo*/NIMS images (Sánchez-Lavega et al. 2017, Figure 3 therein). McGouldrick & Tsang (2017) reported an oscillation of approximately 150 days apparent between 30° S and 60° S on the nightside clouds’ radiance in the $1.74\ \mu\text{m}$ VIRTIS-M images; this timescale is consistent with the cycle of cloud formation and evolution driven by the radiative dynamical feedback and gravitational settling of the clouds’

particles. The analysis of the dayside winds with VMC from 2006 December to 2013 August (~ 1200 days) revealed long-term variations on both components of the wind at $\sim 20^\circ$ S, with the meridional winds exhibiting a gradual increase until its magnitude doubles, while the zonal winds seemed subject to an apparent oscillation of ~ 3 years (Khatuntsev et al. 2017, Figure 11 therein).

In order to perform an analysis of the variability of the zonal winds at the nightside lower clouds using an even longer timescale, we decided to combine data not only from *Akatsuki*/IR2 and *VEx*/VIRTIS, but also from ground-based observations and in situ measurements. Figure 13 shows the variability of the zonal winds at the low latitudes (30° S– 30° N) of the nightside lower clouds from 1978 December to 2017 February (spanning 38 years). The zonal winds during 1978 December (Figure 13(A)) and 1985 June (Figure 13(D)) correspond to the averages of the instantaneous in situ wind measurements between altitudes of 50 to 60 km as provided by the *Pioneer Venus Night Probe* (Counselman et al. 1980) and *VEGA* landers (Moroz & Zasova 1997). To reduce the impact of transient phenomena like equatorial jets, the zonal winds

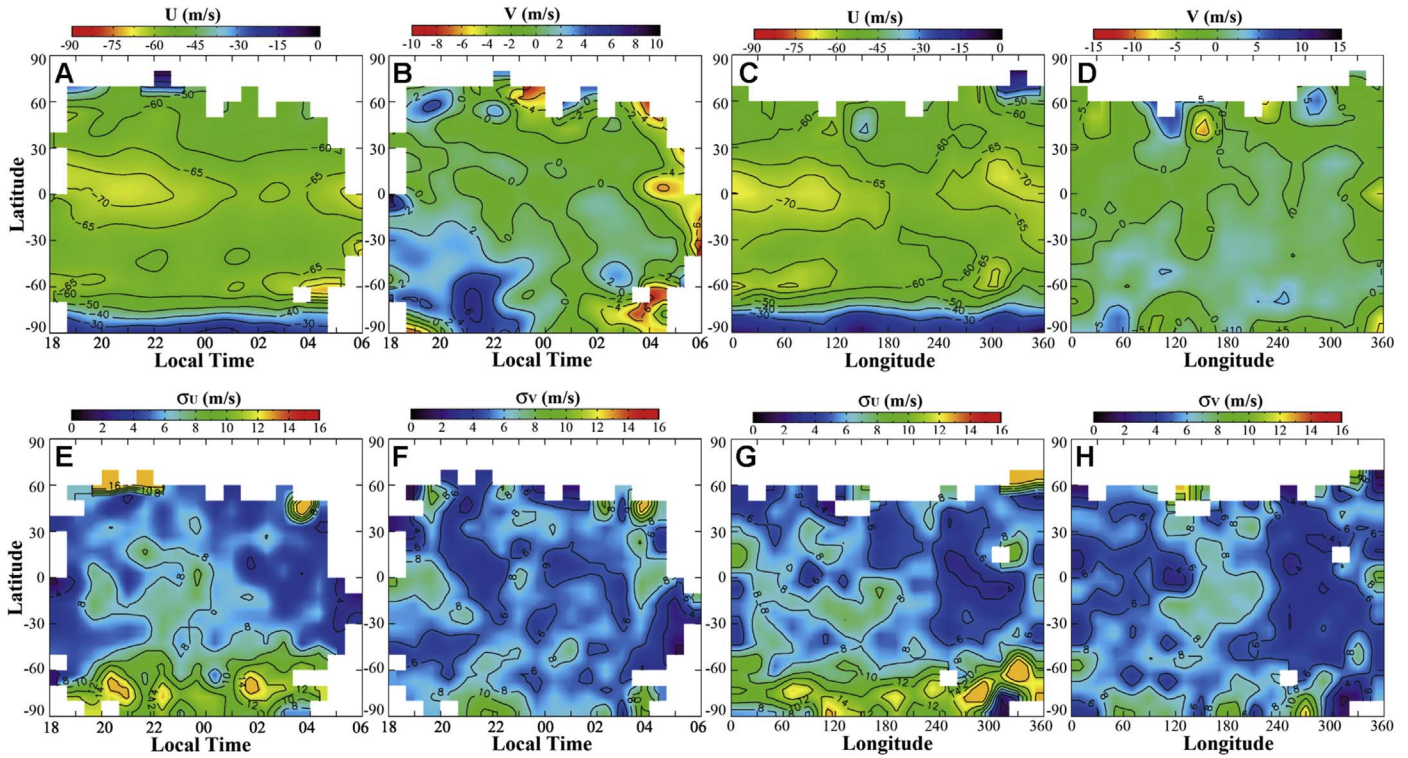


Figure 12. Winds' dependence on the local time and longitude when the measurements from *VEx*/VIRTIS-M (2006–2008) and *Akatsuki*/IR2 (2016) are combined. The averages and standard deviation are calculated for bins of latitude, longitude, and local time of 10° , 10° , and $40'$, respectively. Panels (A)–(D) display the zonal and meridional winds' dependence on the local time and the longitude, while panels (E)–(H) display the corresponding errors. Since the mean zonal winds during 2016 were faster than those during the *VEx* mission (see Figure 5(A)), the zonal speeds used in panels (A) and (C) were multiplied by a correction factor to have comparably zonally averaged profiles.

obtained with cloud tracking are presented as time averages of about 10–20 days in most of the cases, though this value strongly depends on the data availability and how this is distributed along time. Thus, zonal speeds from IRTF/SpeX images correspond to nearly instantaneous winds (several hours) while the average for 2004 May is provided by Limaye et al. (2006) for observations performed over 70 days. The mean zonal winds displayed in Figures 13(A)–(I) were obtained from published results (Counselman et al. 1980; Allen & Crawford 1984; Allen 1987; Crisp et al. 1989, 1991; Carlson et al. 1991; Moroz & Zasova 1997; Chanover et al. 1998; Limaye et al. 2006). The wind speeds from 2006 to 2017 correspond to the revisiting of the *VEx* measurements (Figure 13(J)) by Sánchez-Lavega et al. (2008) and Hueso et al. (2012), and our measurements using *Akatsuki*/IR2 (Figure 13(M)), IRTF/SpeX (Figures 13(L) and (N)), and TNG/NICS (Figure 13(K)).

Although caution must be taken when comparing values from different time averages and images acquired with different filters may provide some discrepancies in the vertical level sensed, Figure 13 suggests that the zonal wind speeds at the nightside lower clouds seem to experience long-term variation of up to 30 m s^{-1} in the intensity of the winds (this total variation is larger than variabilities linked by the local time or longitudinal dependence described in Sections 4.2 and 4.3). The zonal winds display a strong increase from the entry of the *Pioneer Venus* probes in 1978 (Figure 13(A)) and the first cloud-tracked winds with ground-based observations (Figure 13(B)) in the early 1980s. From 1983 to 1990

(Figures 13(B)–(G)), the zonal winds exhibited a gradual decrease in magnitude, while from 2004 to 2008, the zonal winds experienced an increase above the error bars (Figure 13(J) from *VEx* data). This long-term behavior of the nightside zonal winds from VIRTIS-M images diverges from the oscillation between 2007 and 2009 reported in zonal winds between 15°S and 25°S of the dayside middle to lower clouds (Khatuntsev et al. 2017, Figure 11(a) therein). The differences between the altitude range sensed in the day- and nightside images (Sánchez-Lavega et al. 2008; Takagi & Iwagami 2011; Khatuntsev et al. 2017) or the distinct image sampling and time coverage for the winds obtained from VMC and VIRTIS-M may account for this discrepancy between *VEx* results.

The decadal variability for the zonal winds at the lower clouds also retain similarities with the long-term trend for the SO_2 abundance at the cloud tops reported by Marcq et al. (2013) during 30 years of observations combining *Pioneer Venus* and *VEx* observations. The gradual decrease of the zonal winds over 1983–1990 matches the decrease of the SO_2 at the upper clouds (Marcq et al. 2013, Figure 3 therein), which would support the idea that the vertical level sensed by the nightside images at 1.74 , 2.26 , and $2.32 \mu\text{m}$ might be variable. This would make sense if the photochemical activity at the upper clouds could affect the total opacity of the cloud layer (Knollenberg & Hunten 1980; Grinspoon et al. 1993). In such a case, faster zonal speeds may be coincident with periods when higher altitudes can be sensed in the nightside images.

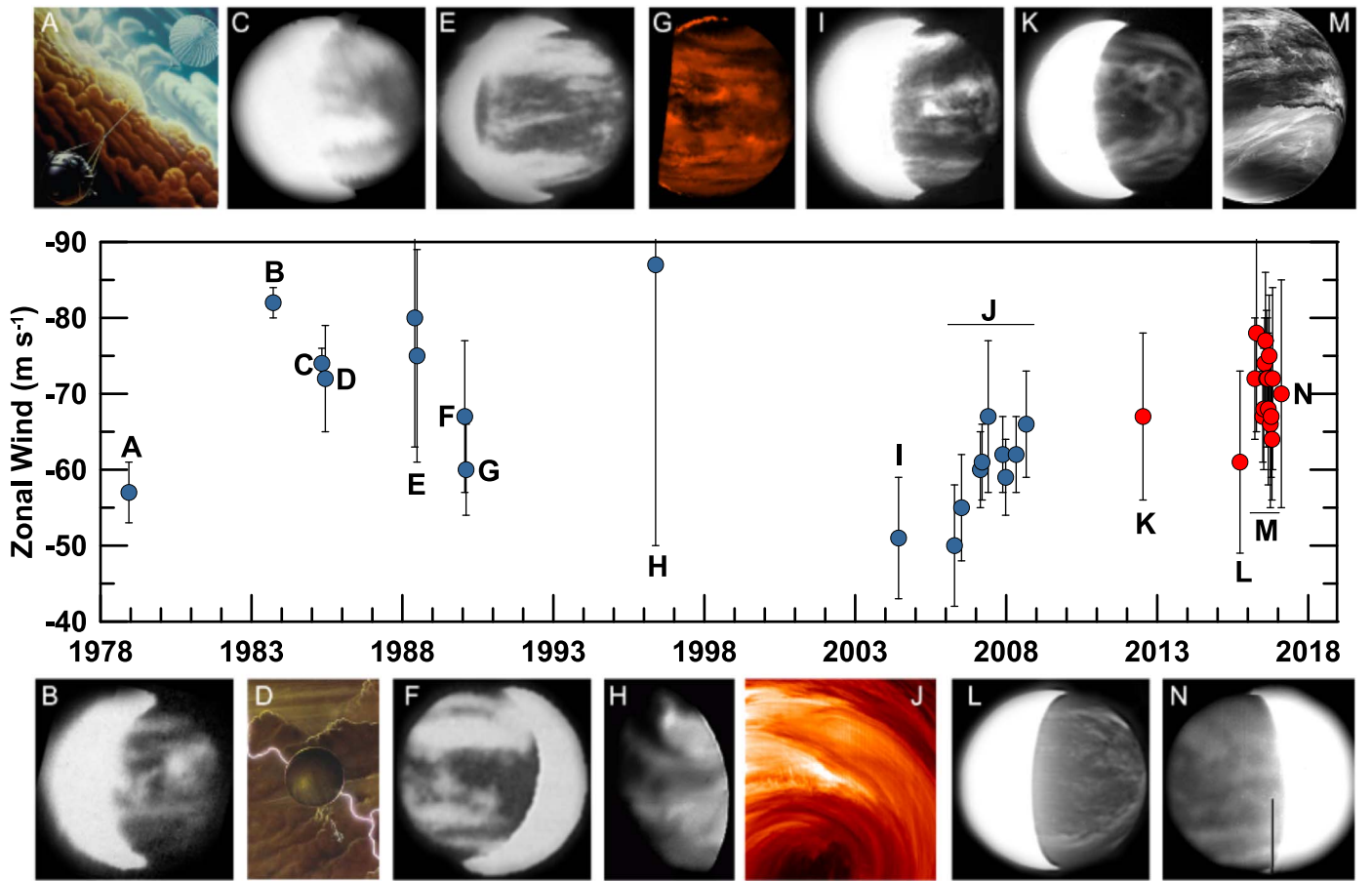


Figure 13. Decadal variation of the zonal winds at the nightside lower clouds of Venus. Data correspond to time averages of the zonal winds obtained between 30°S and 30°N with cloud tracking, except for panels (A) and (D), which represent instantaneous in situ wind measurements from the *Pioneer Venus Night Probe* (Counselman et al. 1980) and *VEGA* landers (Moroz & Zasova 1997) averaged within altitudes of 50–60 km. Blue dots represent time averages using wind speeds provided in previous publications: (A) Counselman et al. (1980), (B) Allen & Crawford (1984), (C) Allen (1987), (D) Moroz & Zasova (1997), (E) Crisp et al. (1989), (F) Crisp et al. (1991), (G) Carlson et al. (1991), (H) Chanover et al. (1998), (I) Limaye et al. (2006), and (J) Hueso et al. (2012). New data presented in this work and based on cloud tracking measurements are shown by the red dots and were obtained from the TNG/NICS (K), IRTF/SpeX (L and N), and *Akatsuki*/IR2 images (M). The error bars stand for the standard deviation of the time averages.

6. Conclusions

We have presented global results of the wind speeds at the nightside lower clouds of Venus during the first year of JAXA's *Akatsuki* mission. Both zonal and meridional winds were obtained by applying cloud tracking techniques to $2.26\text{ }\mu\text{m}$ images acquired by the IR2 camera from a selection of 466 images spanning the time interval from 2016 March 22 to October 31. Automatic and manual measurements were applied independently to obtain 149,033 and 2947 wind vectors, respectively. In the specific case of manual measurements, the phase -correlation technique was tested in the template matching for the first time on Venus with comparable results to those obtained using cross-correlation techniques in the space domain. No dependence is found between the wind speeds and the radiance or the size of the cloud tracers. This supports recent reports of wind variability due to strong horizontal shear and episodes of jets at the equator, and the identification of the clouds' morphology consistent with shear instabilities. The meridional profiles of zonally averaged wind speeds are in overall agreement with the results over 2006–2008 from *VEx* but are systematically 10 m s^{-1} faster. Our results confirm in the northern hemisphere the expected poleward decay of the zonal winds with symmetric winds

between both hemispheres. As opposed to previous observations with *VEx*, zonal speeds during the *Akatsuki* mission exhibit a local maximum in the westward wind speeds caused by either a local time dependence and/or influence of surface elevations, although the irregular coverage of the data set prevents a definitive confirmation of its source. Also, a first analysis of the decadal wind variability is performed for zonal winds between 30°S and 30°N using a combination of in situ and cloud tracking measurements performed between 1978 and 2017. Our results demonstrate yearly and decadal wind variability, suggesting that the zonal winds at low latitudes might be affected by an oscillating disturbance with an amplitude of about $\sim 15\text{ m s}^{-1}$ and a period of about 30 years.

Finally, in order to facilitate future studies of wind variability and data comparison, we provide the full data set of wind measurements using the manual technique, accompanied by the template matching for individual measurements and animations of the projected image sequences used toward this purpose (see the supplemental material and the Appendix).

J.P. acknowledges JAXA's International Top Young Fellowship. R.H. and A.S.-L. were supported by the Spanish MINECO project AYA2015-65041-P with FEDER, UE support, and Grupos

Gobierno Vasco IT-765-13. All authors acknowledge the work of the entire *Akatsuki* team. We are also grateful to the anonymous reviewer for useful comments that improved the manuscript.



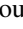


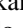





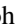
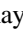

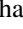
Appendix

Description of the Supplemental Material

The supplemental material that accompanies this work consists of a compressed file that contains not only the numerical values of our manual wind measurements obtained with the images of *Akatsuki*/IR2 camera, but also a large set of images exhibiting the morphology of the cloud tracers and the quality of the template matching and geometrical projections of the IR2 images, and animations of the cloud motions. The contents of the supplemental material are described as follows:

1. A readme file with a more detailed description of the contents of the compressed file, as well as explanations of the naming of files and folders.
2. A Microsoft Excel file and CSV files with the numerical values of the 2277 manual wind measurements and where the motions of the equatorial cloud discontinuity have been filtered out.
3. A total of 103 folders for each pair of IR2 images, with wind measurements, animations, and the cloud tracers' morphology and position.

ORCID iDs

Javier Peralta  <https://orcid.org/0000-0002-6823-1695>
 Ricardo Hueso  <https://orcid.org/0000-0003-0169-123X>
 Takeshi Horinouchi  <https://orcid.org/0000-0002-2296-1975>
 Agustín Sánchez-Lavega  <https://orcid.org/0000-0001-7355-1522>
 Shin-ya Murakami  <https://orcid.org/0000-0002-7137-4849>
 Pedro Machado  <https://orcid.org/0000-0001-6757-5763>
 Eliot F. Young  <https://orcid.org/0000-0001-8242-1076>
 Yeon Joo Lee  <https://orcid.org/0000-0002-4571-0669>
 Toru Kouyama  <https://orcid.org/0000-0002-1060-3986>
 Kevin McGouldrick  <https://orcid.org/0000-0003-0328-649X>
 Takehiko Satoh  <https://orcid.org/0000-0001-9071-5808>
 Sanjay S. Limaye  <https://orcid.org/0000-0001-8659-2104>
 Takao M. Sato  <https://orcid.org/0000-0002-7090-2689>
 Kazunori Ogohara  <https://orcid.org/0000-0001-7666-4442>
 David Luz  <https://orcid.org/0000-0002-9473-8035>

References

- Acton, C. H. 1996, *P&SS*, **44**, 65
 Ahmed, J., & Jafri, M. N. 2008, in *Image and Signal Processing*, ed. A. Elmoataz et al. (Berlin: Springer), 128
 Allen, D. A. 1987, *Icar*, **69**, 221
 Allen, D. A., & Crawford, J. W. 1984, *Natur*, **307**, 222
 Baffa, C., Comoretto, G., Gennari, S., et al. 2001, *A&A*, **378**, 722
 Belton, M. J. S., Gierasch, P. J., Smith, M. D., et al. 1991, *Sci*, **253**, 1531
 Bertaux, J.-L., Khatuntsev, I. V., Hauchecorne, A., et al. 2016, *JGRE*, **121**, 1087
 Bevington, P. R., & Robinson, D. K. 1992, *Data Reduction and Error Analysis for the Physical Sciences* (2nd ed.; New York: McGraw-Hill)
 Blamont, J. E., Young, R. E., Seiff, A., et al. 1986, *Sci*, **231**, 1422
 Carlson, R. W., Baines, K. H., Kamp, L. W., et al. 1991, *Sci*, **253**, 1541
 Chanover, N. J., Glenar, D. A., & Hillman, J. J. 1998, *JGR*, **103**, 31335
 Counselman, C. C., Gourevitch, S. A., King, R. W., Lioriot, G. B., & Ginsberg, E. S. 1980, *JGR*, **85**, 8026
 Crisp, D., McMuldroch, S., Stephens, S. K., et al. 1991, *Sci*, **253**, 1538
 Crisp, D., Sinton, W. M., Hodapp, K.-W., et al. 1989, *Sci*, **246**, 506
 del Genio, A. D., & Rossow, W. B. 1990, *JatS*, **47**, 293
 Fedorova, A., Marcq, E., Luginin, M., et al. 2016, *Icar*, **275**, 143
 Folkner, W. M., Williams, J. G., & Boggs, D. H. 2009, *IPNPR*, **178**, 1
 Foroosh, H., Zerubia, J. B., & Berthod, M. 2002, *ITIP*, **11**, 188
 Fukuhara, T., Futaguchi, M., Hashimoto, G. L., et al. 2017, *NatGe*, **10**, 85
 Gierasch, P. J., Goody, R. M., Young, R. E., et al. 1997, in *The General Circulation of the Venus Atmosphere: an Assessment*, ed. S. W. Bougher, D. M. Hunten, & R. J. Phillips (Tucson, AZ: Univ. Arizona Press), 459
 Gorinov, D. A., Khatuntsev, I. V., Zasova, L. V., Turin, A. V., & Piccioni, G. 2018, *GeoRL*, **45**, 2554
 Grinspoon, D. H., Pollack, J. B., Sitton, B. R., et al. 1993, *P&SS*, **41**, 515
 Hahn, G., & Jacquesson, M. 2012, *WinJUPOS-Database for object positions on planets and the Sun*, <http://jupos.privat.t-online.de>
 Horinouchi, T., Kouyama, T., Lee, Y. J., et al. 2018, *EP&S*, **70**, 10
 Horinouchi, T., Murakami, S., Satoh, T., et al. 2017a, *NatGe*, **10**, 646
 Horinouchi, T., Murakami, S.-y., Kouyama, T., et al. 2017b, *MeScT*, **28**, 085301
 Huang, H., Yoo, S., Yu, D., Huang, D., & Qin, H. 2012, in *Proc. Twelfth Int. Workshop on Multimedia Data Mining, MDMKDD '12* (New York: ACM), 1
 Hueso, R., Peralta, J., Garate-Lopez, I., Bandos, T. V., & Sánchez-Lavega, A. 2015, *P&SS*, **113**, 78
 Hueso, R., Peralta, J., & Sánchez-Lavega, A. 2012, *Icar*, **217**, 585
 Humblot, F., Collin, B., & Mohammad-Djafari, A. 2005, in *Physics in Signal and Image Processing (PSIP) conf.*, PSIP '05, 115
 Ikegawa, S., & Horinouchi, T. 2016, *Icar*, **271**, 98
 Iwagami, N., Sakano, T., Hashimoto, G. L., et al. 2018, *EP&S*, **70**, 6
 Jun, L., & Fengxian, Z. 1992, *AdSpR*, **12**, 123
 Khatuntsev, I. V., Patsaeva, M. V., Titov, D. V., et al. 2013, *Icar*, **226**, 140
 Khatuntsev, I. V., Patsaeva, M. V., Titov, D. V., et al. 2017, *JGRE*, **122**, 2312
 Knollenberg, R. G., & Hunten, D. M. 1980, *JGR*, **85**, 8039
 Kouyama, T., Imamura, T., Nakamura, M., Satoh, T., & Futaana, Y. 2012, *P&SS*, **60**, 207
 Kouyama, T., Imamura, T., Nakamura, M., Satoh, T., & Futaana, Y. 2013, *JGRE*, **118**, 37
 Kouyama, T., Imamura, T., Taguchi, M., et al. 2017, *GeoRL*, **44**, 12,098
 Kuglin, C. D. 1975, in *Proc. Int. Conf. on Cyber-netics Society*, 163, <https://ci.nii.ac.jp/naid/20001697044/en/>
 Kuglin, C. D. 1976, *Performance of the Phase Correlator in Image Guidance Applications*, Tech. Rep., Control Data Corp Minneapolis MN Image Systems DIV (Palo Alto, California: Palo Alto Research Lab., Lockheed Missiles and Space Company, Inc.)
 Lee, Y. J., Imamura, T., Schröder, S. E., & Marcq, E. 2015a, *Icar*, **253**, 1
 Lee, Y. J., Sawaga, H., Sato, T. M., et al. 2017a, in *Abstracts of JpGU-AGU Joint Meeting 2017*, PPS06-P18
 Lee, Y. J., Titov, D. V., Ignatiev, N. I., et al. 2015b, *P&SS*, **113**, 298
 Lee, Y. J., Yamazaki, A., Imamura, T., et al. 2017b, *AJ*, **154**, 44
 Leese, J. A., Novak, C. S., & Taylor, V. R. 1970, *Pattern Recognition*, **2**, 279
 Limaye, S., Warell, J., Bhatt, B. C., Fry, P. M., & Young, E. F. 2006, *BASI*, **34**, 189
 Limaye, S. S. 2007, *JGRE*, **112**, E04S09
 Limaye, S. S., Watanabe, S., Yamazaki, A., et al. 2018, *EP&S*, **70**, 38
 Marcq, E., Bertaux, J.-L., Montmessin, F., & Belyaev, D. 2013, *NatGe*, **6**, 25
 McGouldrick, K., Baines, K. H., Momary, T. W., & Grinspoon, D. H. 2008, *JGRE*, **113**, E00B14
 McGouldrick, K., Momary, T. W., Baines, K. H., & Grinspoon, D. H. 2012, *Icar*, **217**, 615
 McGouldrick, K., & Toon, O. B. 2007, *Icar*, **191**, 1
 McGouldrick, K., & Toon, O. B. 2008, *Icar*, **196**, 35
 McGouldrick, K., & Tsang, C. C. C. 2017, *Icar*, **286**, 118
 Moroz, V. I., & Zasova, L. V. 1997, *AdSpR*, **19**, 1191
 Mota Machado, P., Peralta, J., Luz, D., et al. 2016, *AAS/DPS Meeting 48 Abstracts*, 115.06
 Nakamura, M., Imamura, T., Ishii, N., et al. 2016, *EP&S*, **68**, 1
 Ogohara, K., Kouyama, T., Yamamoto, H., et al. 2012, *Icar*, **217**, 661
 Ogohara, K., Takagi, M., Murakami, S.-y., et al. 2017, *EP&S*, **69**, 167
 Parish, H. F., Schubert, G., Covey, C., et al. 2011, *Icar*, **212**, 42
 Peralta, J., Hueso, R., & Sánchez-Lavega, A. 2007, *Icar*, **190**, 469
 Peralta, J., Hueso, R., Sánchez-Lavega, A., et al. 2017a, *NatAs*, **1**, 0187
 Peralta, J., Imamura, T., Read, P. L., et al. 2017b, *GeoRL*, **44**, 3907
 Peralta, J., Lee, Y. J., Hueso, R., et al. 2017c, *Icar*, **288**, 235
 Peralta, J., Luz, D., Berry, D. L., et al. 2012, *Icar*, **220**, 958
 Piccioni, G., Drossart, P., Suetta, E. et al. (ed.) 2007, in *ESA Special Publication 1295, VIRTIS: The Visible and Infrared Thermal Imaging Spectrometer* (Noordwijk: ESA)
 Rayner, J. T., Toomey, D. W., Onaka, P. M., et al. 2003, *PASP*, **115**, 362
 Reddy, B. S., & Chatterji, B. N. 1996, *ITIP*, **5**, 1266

- Rossow, W. B., del Genio, A. D., & Eichler, T. 1990, *JAtS*, **47**, 2053
- Samritjarapon, O., & Chitsobhuk, O. 2008, IEEE, Int. Symp. Communications and Information Technologies, 364
- Sánchez-Lavega, A., Hueso, R., Piccioni, G., et al. 2008, *GeoRL*, **35**, 13204
- Sánchez-Lavega, A., Lebonnois, S., Imamura, T., Read, P., & Luz, D. 2017, *SSRv*, **212**, 1541
- Satoh, T., Nakamura, M., Ueno, M., et al. 2016, *EP&S*, **68**, 74
- Satoh, T., Sato, T. M., Nakamura, M., et al. 2017, *EP&S*, **69**, 154
- Schubert, G. 1983, in General Circulation and the Dynamical State of the Venus Atmosphere, ed. D. M. Hunten et al. (Tucson, AZ: Univ. Arizona Press), 681
- Takagi, M., Sugimoto, N., Ando, H., & Matsuda, Y. 2018, *JGRE*, **123**, 335
- Takagi, S., & Iwagami, N. 2011, *EP&S*, **63**, 435
- Tavenner, T., Young, E. F., Bullock, M. A., Murphy, J., & Coyote, S. 2008, *P&SS*, **56**, 1435
- Titov, D. V., Svedhem, H., Koschny, D., et al. 2006, *P&SS*, **54**, 1279